

Blue-green luminescence properties and energy transfer in Tm^{3+}/Tb^{3+} co-doped TeO_2-GeO_2-Bi_2O_3-BaF_2 glass

Ruizhen Pang(庞瑞祯), Tong Wu(吴童), Kexuan Han(韩科选),Zhenyu Zhou(周振宇), and Wei Zheng(郑威)
Citation: Chin. Phys. B, 2026, 35 (**7**): 077801. DOI: 10.1088/1674-1056/ae12d0
http://cpb.iphy.ac.cn; http://iopscience.iop.org/cpb

What follows is a list of articles you may be interested in

Structural phase transition and quasi-layered active-ion distribution suppress concentration quenching in Tb^{3+}-activated $KBi(MoO_4)_2$

Mengyu Zhang(张梦宇), Shujing Pan(潘淑晶), Haitang Hu(胡海棠), Wenzhi Su(宿文志), Yong Zou(邹勇), Shoujun Ding(丁守军), and Qingli Zhang(张庆礼)
Chin. Phys. B, 2026, 35 (**1**): 017801. DOI: 10.1088/1674-1056/ae1c25

Luminescent characteristics of $Tm^{3+}/Tb^{3+}/Eu^{3+}$ tri-doped $Na_5Y_9F_{32}$ single crystals for white emission with high thermal stability

Lizhi Fang(方立志), Xiong Zhou(周雄), Zhiwei Zhao(赵志伟), Biao Zheng(郑标), Haiping Xia(夏海平), Jun Wang(王军), Hongwei Song(宋宏伟), and Baojiu Chen(陈宝玖)
Chin. Phys. B, 2022, 31 (**12**): 127802. DOI: 10.1088/1674-1056/ac6160

Tuning energy transfer efficiency in quantum dots mixture by controling donor/acceptor ratio

Chang Liu(刘畅), Jing Liang(梁晶), Fangfang Wang(王芳芳), Chaojie Ma(马超杰), Kehai Liu(刘科海), Can Liu(刘灿), Hao Hong(洪浩), Huaibin Shen(申怀彬), Kaihui Liu(刘开辉), and Enge Wang(王恩哥)
Chin. Phys. B, 2021, 30 (**12**): 127802. DOI: 10.1088/1674-1056/ac29b2

Investigation of fluorescence resonance energy transfer ultrafast dynamics in electrostatically repulsed and attracted exciton-plasmon systems

Hong-Yu Tu(屠宏宇), Ji-Chao Cheng(程基超), Gen-Cai Pan(潘根才), Lu Han(韩露), Bin Duan(段彬), Hai-Yu Wang(王海宇), Qi-Dai Chen(陈岐岱), Shu-Ping Xu(徐抒平), Zhen-Wen Dai(戴振文), and Ling-Yun Pan(潘凌云)
Chin. Phys. B, 2021, 30 (**2**): 027802. DOI: 10.1088/1674-1056/abb802

The effects of Er^{3+} ion concentration on 2.0-μ m emission performance in Ho^{3+}/Tm^{3+} co-doped $Na_5Y_9F_{32}$ single crystal under 800-nm excitation

Benli Ding(丁本利), Xiong Zhou(周雄), Jianli Zhang(章践立), Haiping Xia(夏海平), Hongwei Song(宋宏伟), and Baojiu Chen(陈宝玖)
Chin. Phys. B, 2021, 30 (**1**): 017801. DOI: 10.1088/1674-1056/abaede

---

Blue–green luminescence properties and energy transfer in Tm^{3+}/Tb^{3+} co-doped TeO_2–GeO_2–Bi_2O_3–BaF_2 glass

Ruizhen Pang(庞瑞祯)[1,†], Tong Wu(吴童)[3,†], Kexuan Han(韩科选)[1,2,‡], Zhenyu Zhou(周振宇)[1], and Wei Zheng(郑威)[1]

[1] *School of Materials Science and Engineering, Changchun University of Science and Technology, Changchun* 130022, *China*
[2] *Chongqing Research Institute, Changchun University of Science and Technology, Chongqing* 401120, *China*
[3] *CDGM GLASS Co., Ltd., Chengdu* 610100, *China*

(Received 21 July 2025; revised manuscript received 9 September 2025; accepted manuscript online 14 October 2025)

Tm^{3+}/Tb^{3+} co-doped TeO_2–GeO_2–Bi_2O_3–BaF_2 glasses were synthesized via high-temperature melt-quenching to achieve blue–green fluorescence emission. Under 808-nm pump excitation, the TGBB2 sample (Tm_2O_3:Tb_4O_7 = 3 : 8) exhibited balanced emissions at 452 nm (blue, Tm^{3+}: $^1G_4 \rightarrow {}^3H_6$) and 544 nm (green, Tb^{3+}: $^5D_4 \rightarrow {}^7F_5$). With increasing Tb^{3+} concentration, green emission intensity increased while blue emission decreased, confirming efficient $Tm^{3+} \rightarrow Tb^{3+}$ energy transfer. Key performance metrics for TGBB2 included: a forward energy transfer coefficient of 571.83×10^{-40} cm^6/s (far exceeding the reverse coefficient of 63.12×10^{-40} cm^6/s), an energy transfer efficiency of 99.5%, maximum emission cross-sections of 5.87×10^{-21} cm^2 (476 nm, Tm^{3+}) and 3.37×10^{-21} cm^2 (486 nm, Tb^{3+}), and corresponding gain coefficients of 2.98 cm^{-1} and 0.46 cm^{-1}. These results validate the glass's low laser threshold, making Tm^{3+}/Tb^{3+} co-doped tellurite–germanate–bismuthate glass a promising candidate for blue–green laser communication and underwater optical transmission.

Keywords: Tm^{3+}/Tb^{3+} co-doping, tellurite–germanate–bismuthate glass, blue–green wavelength band, energy transfer

PACS: 78.55.–m, 81.05.Kf, 71.55.–i, 42.55.–f

DOI: 10.1088/1674-1056/ae12d0 **CSTR:** 32038.14.CPB.ae12d0

1. Introduction

Amidst the rapid pace of technological evolution, the ocean, Earth's most resource-abundant yet least explored realm, has seen a surge in research and development endeavors. Within the domain of marine resource exploration, a pressing need exists for reliable and efficient underwater communication technologies. This requirement encompasses deep-sea mineral harvesting, oil and gas exploitation, long-term climate change monitoring, marine ecosystem health evaluation, and underwater military maneuvers. These technologies function not only as indispensable facilitators for resource development and environmental research but also as fundamental pillars for guaranteeing the efficacy of underwater operations.[1,2] Investigations into seawater transmission windows have disclosed that blue–green light within the wavelength range of 440 nm–550 nm displays the greatest transparency in seawater, thereby propelling the rapid advancement of underwater wireless optical communication (UWOC).[3–6] When compared to traditional underwater fiber-optic wired communication, UWOC presents several distinct advantages: cost-effectiveness, high-bandwidth capacity, high-speed information transmission, and heightened security owing to the inherent confidentiality of blue–green light waves in water, which minimizes the risk of information interception. These attributes have established blue–green light UWOC as a prominent area of focus for researchers.

According to recent investigations in matrix materials and doping methodologies, a multitude of rare-earth ions are capable of achieving laser emission within the blue–green spectral region, with Pr^{3+}, Eu^{2+}, Dy^{3+}, Er^{3+}, Tm^{3+}, and Tb^{3+} being the primary candidates.[7] Among them, Pr^{3+} is able to generate blue–green light via upconversion luminescence; however, its extreme susceptibility to the phonon energy of matrix materials and the preparation conditions severely limits its practical applications.[8] As a prospective blue-light activator, Eu^{2+} encounters significant preparation hurdles: europium predominantly exists in the Eu^{3+} state, necessitating the use of reducing agents during synthesis to facilitate the formation of Eu^{2+}, and the complete conversion from Eu^{3+} to Eu^{2+} remains a formidable task. Furthermore, cross-relaxation between Eu^{3+} and Eu^{2+} causes the emission spectrum to shift towards red light, substantially impeding efficient blue-light emission, which represents a crucial scientific challenge that demands urgent resolution.[9] Dy^{3+} displays a high absorption cross-section in the ultraviolet (UV) region, but the low blue-light emission branching ratio constrains the improve-

[†]These authors contributed equally to this work.
[‡]Corresponding author. E-mail: hankexuan@cust.edu.cn

© 2026 Chinese Physical Society and IOP Publishing Ltd. All rights, including for text and data mining, AI training, and similar technologies, are reserved.

ment of lasing efficiency within the blue spectral band.[10] In the case of Er^{3+}, while green emission can be realized through upconversion three-photon absorption, the $^2P_{3/2}$ energy level associated with green emission has an extremely brief lifetime (nanosecond order), thereby preventing sufficient energy accumulation required for population inversion and rendering it less than ideal as a high-gain green activator.[11] Conversely, Tm^{3+} is characterized by a large absorption cross-section at 358 nm, enabling it to directly emit 458-nm blue light upon absorption of UV light at this wavelength. Nonetheless, severe fluorescence quenching takes place at high Tm^{3+} doping concentrations, resulting in a drastic reduction of emission intensity.[12] Tb^{3+} displays intense green emission at 488 nm and 545 nm; however, its low UV absorption cross-section restricts the luminescence intensity. In order to attain efficient Tb^{3+} emission, Tm^{3+} is incorporated to transfer UV pump energy to Tb^{3+}: the high degree of energy-level matching between Tm^{3+} ($^1G_4$) and Tb^{3+} ($^5D_4$) facilitates effective energy transfer through Tm^{3+}/Tb^{3+} co-doping, simultaneously producing blue–green output.[13]

Compared with traditional blue–green light-emitting devices (*e.g.*, high-power blue light-emitting diodes, LEDs), rare-earth ion-doped glass lasers offer the following irreplaceable advantages: (i) Tunable and balanced blue–green emission. High-power blue–green LEDs are constrained by their material bandgap, enabling only fixed single-wavelength emission (*e.g.*, 450-nm blue light, 520-nm green light) and thus failing to match the dynamically varying seawater transmission window. In rare-earth-doped glasses, the emission intensities of blue light (452 nm) and green light (544 nm) can be continuously tuned by adjusting the doping ratio of rare-earth ions. For instance, in this study, such tuning is achieved by modifying the doping ratio of Tm^{3+} to Tb^{3+}. This capability allows the material to adapt to diverse seawater environments and optimize transmission rates. (ii) Superior compatibility with optical fiber integration. Direct blue–green light-emitting devices, particularly LEDs, possess a large emission divergence angle ($> 120°$), which hinders their integration with optical fibers and results in coupling losses exceeding 30%.[14] In contrast, the glass developed in this work exhibits a high refractive index (1.8341 in this study), which matches that of commercial silica optical fibers. Furthermore, its excellent glass-forming ability enables the fabrication of fiber preforms via the rod-in-tube method, supporting long-distance fiber-assisted underwater wireless optical communication (UWOC). (iii) Low laser threshold and high energy conversion efficiency. High-power blue–green semiconductor lasers require a high injection current (> 1 A) to achieve lasing, leading to substantial power consumption and heat generation.[15] By contrast, rare-earth ion-doped glasses exhibit a low laser threshold, attributed to their high emission cross-sections and efficient energy transfer efficiencies.[16] This low threshold facilitates the miniaturization of underwater communication systems and reduces their power consumption, making the material suitable for portable underwater equipment.

Previously, laser emission in diverse wavelength bands was successfully achieved by our research group utilizing various glass systems, such as tellurite,[17] germanate,[18] and bismuthate glass.[19] Tellurite glass, a typical heavy-metal oxide system, assumes an indispensable role in laser applications owing to its high refractive index and low phonon energy.[20] Nevertheless, akin to other heavy-metal oxide glasses, tellurite glass is incapable of forming a vitreous structure solely from pure TeO_2; the incorporation of appropriate network intermediates and modifiers is imperative for promoting glass formation.[21] Germanate glass, on the contrary, displays stable glass-forming capability and a wide transmission range,[22] and it provides superior thermal stability and reliable mechanical properties when compared with fluoride glass.[23] Bismuthate glass is characterized by its prominent refractive index, hardness, and third-order nonlinear refractive index.[24] It is noteworthy that the hydroxyl (OH) content in glass has a significant impact on fluorescence emission intensity, whereas the introduction of fluorides (*e.g.*, BaF_2) can efficiently decrease the OH^- concentration.[25] Moreover, fluorides reduce the melting point of the glass and the maximum phonon energy, increase the solubility of rare-earth ions, and consequently minimize non-radiative energy loss during the transfer process, leading to an improvement in quantum efficiency.[26]

Therefore, in the present study, GeO_3 and Bi_2O_3 were introduced into a traditional tellurite glass system to fabricate a TeO_2–GeO_3–Bi_2O_3–BaF_2 glass system. Tm^{3+}/Tb^{3+}-co-doped TeO_2–GeO_3–Bi_2O_3–BaF_2 glass was synthesized through high-temperature melt-quenching, thereby achieving blue–green laser emission within the wavelength range of 440 nm–550 nm. The physical properties and microstructure of the matrix glass were characterized using x-ray diffraction (XRD), Raman spectroscopy, and differential thermal analysis. Absorption and fluorescence spectra, along with fluorescence lifetimes, were measured in the Tm^{3+}/Tb^{3+} co-doping experiments. Radiative parameters, emission cross-sections, energy transfer coefficients, and quantum efficiency were calculated by employing theoretical frameworks such as Judd–Ofelt, McCumber, and Dexter theories, thereby facilitating the analysis of the $Tm^{3+} \rightarrow Tb^{3+}$ sensitization effect and energy transfer mechanism. The results indicate that Tm^{3+}/Tb^{3+}-co-doped tellurium–germanium–bismuthate glass exhibits broad application prospects in optical communications.

2. Experimental details

2.1. Glass sample preparation

In the present experimental work, high-purity (99.99%) raw materials comprising TeO_2, GeO_3,Bi_2O_3, BaF_2, Tm_2O_3, and Tb_4O_7 were employed to synthesize Tm^{3+}/Tb^{3+}-co-doped TeO_2–GeO–Bi_2O_3–BaF_2 glass samples through high-temperature melt-quenching. The glass composition for Tm^{3+}/Tb^{3+} co-doping was formulated as $70TeO_2$–$5GeO_2$–$5Bi_2O_3$–$20BaF_2$–$0.75Tm_2O_3$-xTb_4O_7 (x = 1, 2, 3, 4, 5 mol%), designated sequentially as TGBB1, TGBB2, TGBB3, TGBB4, and TGBB5, with rare-earth ions (Tm^{3+} and Tb^{3+}) introduced as extrinsic dopants. The matrix glass having a composition of $70TeO_2$–$5GeO_2$–$5Bi_2O_3$–$20BaF_2$ was designated as TGBB. The preparation procedure was as follows: 10 g of raw materials were precisely weighed according to the formulation, ground in an agate mortar for 15 min within a dry environment to ensure homogeneous mixing, transferred into a corundum crucible, and heated at 950 °C for 30 min in a resistance furnace under ambient air with a crucible lid to mitigate volatilization of TeO_2 and BaF_2. Subsequently, the molten glass was poured onto a preheated copper plate. It underwent annealing in a muffle furnace at 370 °C for 8 hours to alleviate thermal stress and enhance mechanical strength, followed by natural cooling to room temperature. Finally, all glass samples, including TGBB1–TGBB4 used for fluorescence measurements, were sequentially ground with 800#–3000# silicon carbide sandpapers and subsequently polished with 1-μm alumina polishing paste. This processing resulted in optical-grade double-sided polishing and uniform dimensions of 10 mm×10 mm×2 mm (length×width×thickness), with surface flatness and roughness verified via a laser interferometer. All processed glass samples were then used for the subsequent characterization and analysis of physicochemical properties and spectral properties. Photographs of all glass samples are presented in Fig. 1.

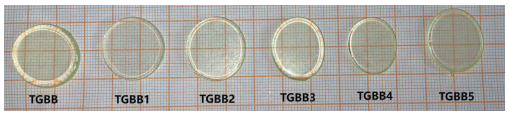


Fig. 1. Glass samples of TGBB and TGBB1-TGBB5.

2.2. Measurement methods and instrument

The density of the matrix glass TGBB was determined to be 4.9702 g/cm^3 via Archimedes' displacement method, with distilled water serving as the immersion medium, whereas the doped sample TGBB2 had a density of 5.0629 g/cm^3. The refractive index of the matrix glass at 587 nm was measured to be 1.8341 by means of a Horiba France SAS ellipsometer, with the Abbe number calculated as 23.23 and the measurement resolution set at 1 nm. The x-ray diffraction (XRD) measurements of the glass samples were performed using a Rigaku diffractometer with a step size of 0.02°, a 2θ scanning range of 10°–80°, and a scanning rate of 10°/min. A Horiba LabRAM HR evolution spectrometer was used to obtain Raman spectra from 100 cm^{-1} to 1000 cm^{-1} at 1-cm^{-1} intervals, with a 488-nm laser diode (LD) serving as the excitation source. Thermal properties were characterized using a Netzsch DSC214 differential scanning calorimeter under an N_2 atmosphere, with the temperature scanned from room temperature to 600 °C at a heating rate of 5 °C/min. Absorption spectra of Tm^{3+}/Tb^{3+} co-doped glasses were recorded using a PerkinElmer Lambda 950 UV–Vis spectrophotometer with 2-mm-thick sample slices. Fluorescence spectra and rare-earth ion fluorescence lifetimes were measured with a Hitachi F4600 spectrofluorometer, excited by a 488-nm laser diode (LD) at 1-W power, and the signals were detected by a liquid-nitrogen-cooled PbSe detector.

3. Results and discussion

3.1. Glass structure and physical property characterization

Before the present investigation, the physical properties of Tb^{3+}-doped matrix glass were investigated by our group, with the densities of the matrix glass and Tb^{3+}-monodoped glass determined to be 4.9702 g/cm^3 and 5.0846 g/cm^3, respectively, using Archimedes' displacement method. The density of the TGBB2 sample was determined to be 5.0629 g/cm^3, as tabulated in Table 1. Notably, the incorporation of rare-earth ions led to a noticeable increase in the density of the glass when compared to the matrix glass (TGBB).

Table 1. Densities of the matrix glass and rare-earth-doped glass (g/cm^3).

Glass sample	TGBB	T5[27]	TGBB2
Density	4.9702	5.0846	5.0629

The refractive index of the matrix glass TGBB at 587 nm was found to be 1.8341 by means of Sellmeier function fitting, and the Abbe number was calculated as 23.23.[27] The data in the range of 1000 nm–2000 nm were obtained by fitting the second-order Sellmeier equation. The second-order Sellmeier equation is shown in the following equation:

$$n^2 = 1 + A_0 + \sum_{n=1}^{2} \frac{A_n \lambda^2}{\lambda^2 - a_n^2}, \tag{1}$$

where λ is the wavelength, A_0, A_n, a_n are the Sellmeier coefficients $A_0 = 1.0524$, $A_1 = 0.5812$, $A_2 = 0.5813$, $a_1 = 185.3603$ nm^2, $a_2 = 185.3417$ nm^2.

The degree of chromatic dispersion of a glass sample can be expressed in terms of the Abbe number (v_d), calculated as follows:[28]

$$v_d = \frac{n_d - 1}{n_F - n_c}, \tag{2}$$

where n_F, n_d, and n_c are the refractive indices at 486 nm, 587 nm, and 656 nm, respectively, which are 1.8625, 1.8341, and 1.8266.

The thermal stability attributes of the glass specimens were assessed through an analysis of their DSC curves. In previous studies,[27] the DSC curve of the matrix glass TGBB was plotted, indicating a glass transition temperature (T_g) of 396 °C, a crystallization onset temperature (T_x) of 513 °C, and a crystallization peak temperature (T_p) of 535 °C.

To assess the thermal stability of the glass, Dietzel,[29] Saad,[30] and Hruby[31] have proposed three parameters: the temperature difference parameter ΔT, the Saad parameter S, and the Hruby parameter K_H, with their calculation formulas as follows:

$$\Delta T = T_x - T_g, \tag{3}$$

$$S = \frac{(T_p - T_x)(T_x - T_g)}{T_g}, \tag{4}$$

$$K_H = \frac{T_x - T_g}{T_m - T_x}. \tag{5}$$

In the equations above, T_m represents the melting temperature of the glass sample (950 °C). It is widely acknowledged that higher values of ΔT, S, and K_H correlate with greater devitrification resistance and superior glass-forming capability. The thermal stability parameters calculated for the TGBB matrix glass are tabulated in Table 2. Notably, the matrix glass shows a ΔT value of 117 °C, which surpasses those of traditional fluoride (76 °C),[32] bismuthate (88 °C, 102 °C),[33,34] and tellurite (88.43 °C)[35] glass systems. Furthermore, when ΔT exceeds 100 °C, the glass exhibits exceptional thermal stability, providing benefits for optical fiber fabrication.

Table 2. Thermodynamic parameters of the matrix glass TGBB.

Thermodynamic parameters	Calculated value
ΔT (°C)	117
S (K)	3.85
K_H	0.27

Figure 2 depicts the XRD patterns of the matrix glass TGBB and Tm^{3+}/Tb^{3+}-co-doped glass sample TGBB2, which were measured over a diffraction angle range of 10°–80° at a scanning rate of 10°/min. The patterns display no distinct crystalline diffraction peaks but rather broad humps at $2\theta = 26°$ and 49°, thereby confirming that all as-prepared glass samples are in an amorphous (non-crystalline) state. Notably, the TGBB glass exhibits two broad diffraction maxima at $\sim 26°$ and $\sim 29°$ 2θ (angle range of 20°–30°) instead of a single hump. This split arises from the coexistence of distinct short-range structural units in the multi-component matrix: [TeO_4]/[TeO_3] units (from TeO_2) contribute to the $\sim 26°$ peak, while [GeO_4] and [BiO_3]/[BiO_6] units (from GeO_2 and Bi_2O_3) give rise to the $\sim 29°$ peak. The broad nature of both peaks confirms the absence of long-range crystalline order. This phenomenon is characteristic of multi-component amorphous glasses with complex short-range order, distinct from single-component amorphous systems.[23,25]

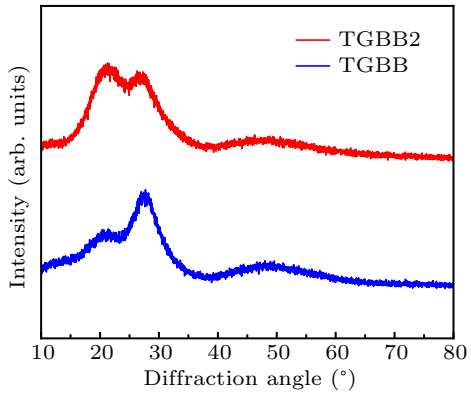


Fig. 2. X-ray diffraction patterns of the glass samples TGBB and TGBB2.

Raman spectroscopy is used to characterize glass structural groups, key chemical bonds, and the maximum phonon energy of the glass matrix. To analyze the glass structure in detail, the Raman spectrum of the matrix glass TGBB is presented in Fig. 3, which shows the Raman spectrum of the matrix glass TGBB, which was excited at 488 nm over the range of 100 cm^{-1}–1000 cm^{-1} and processed via Gaussian peak fitting. Five Raman peaks were identified, and their formation mechanisms are listed in Table 3.

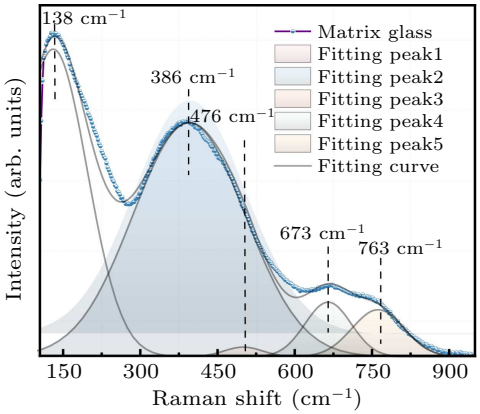


Fig. 3. Raman spectrum of the matrix glass TGBB.

Table 3. Formation mechanisms of the fitted Raman peaks.

Determine the fitted peak wavelength (cm^{-1})	Related functional groups or chemical bonds	References
138	boson peak	[36]
386	[BiO_3] and [BiO_6]	[37]
476	Te–O–Te and O–Te–O	[38]
673	[TeO_4] and [TeO_3]	[39]
763	[TeO_3], [TeO_{3+1}], and [GeO_4]	[40,41]

The fitted peak at 138 cm^{-1} is identified as a boson peak, which can be observed in nearly all glass materials.[36] The peak at 386 cm^{-1} is assigned to vibrations of Bi^{3+},[37] with

Bi^{3+} typically existing as [BiO_3] tetrahedra and [BiO_6] octahedra in the glass network. The peak at 476 cm^{-1} is attributed to the combined vibrations of Te–O–Te and O–Te–O linkages.[38] The peak at 673 cm^{-1} corresponds to the stretching vibrations of Te–O bonds in the trigonal bipyramids of [TeO_4] and [TeO_3] structural units.[39] The fitted peak at approximately 763 cm^{-1} is attributed to the vibrations of Te–O bonds in [TeO_3] and [TeO_{3+1}] structural units,[40] along with the formation of [GeO_4] structural units induced by the incorporation of GeO_2.[41] It is widely recognized that the presence of [TeO_3] and [TeO_{3+1}] units in tellurite glass is essential for stable glass formation, thus confirming that the as-prepared matrix glass TGBB displays strong glass-forming capability. Furthermore, the highest-frequency fitted peak corresponds to the maximum phonon energy of the matrix glass. Thus, the phonon energy of the as-prepared TGBB matrix glass is 763 cm^{-1}, which is significantly lower than that of bismuthate glass (1252 cm^{-1}),[42] borate glass (1200 cm^{-1}–1300 cm^{-1}),[43] and phosphate glass (1290 cm^{-1}).[44] This suggests that the glass is an ideal material for laser emission. A lower maximum phonon energy decreases the proportion of non-radiative relaxation in rare-earth-doped glass, thereby facilitating efficient energy transfer and enhancing light emission at specific wavelengths.[45]

3.2. Optical properties and Judd–Ofelt theoretical analysis

The absorption spectra of the TGBB1–TGBB5 glass samples are illustrated in Fig. 4. These spectra were measured at ambient temperature across a wavelength spectrum spanning 400 nm to 2500 nm. Two groups of absorption peaks are evident: the four characteristic peaks at 488 nm, 1854 nm, 1974 nm, and 2235 nm correspond to Tb^{3+} transitions from the ground state $^7F_6$ to the excited states $^5D_4$, $^7F_1$, $^7F_2$, and $^7F_3$,[46] whereas another five peaks at 473 nm ($^1G_4$), 689 nm ($^7F_{2,3}$), 792 nm ($^3H_4$), 1192 nm ($^3H_5$), and 1740 nm ($^3F_4$) correspond to Tm^{3+} transitions from the ground state $^3H_6$ to the excited states $^1G_4$, $^7F_{2,3}$, $^3H_4$, $^3H_5$, and $^3F_4$.[47] The energy level transitions corresponding to the absorption peaks are labeled in Fig. 4(a). Notably, all peaks represent linear superpositions of the single-doped spectra without significant positional shifts, indicating the uniform dissolution of Tb^{3+} ions in the matrix glass. Additionally, no absorption bands in the wavelength region below 300 nm were identified, attributed to the intrinsic bandgap absorption characteristics of the matrix glass.[48] Fig. 4(b) demonstrates the intensity of the $^7F_6 \rightarrow {}^7F_1$ transition peak as a function of Tb^{3+} doping concentration. With a constant Tm^{3+} concentration of 0.75 mol%, the absorption intensity rises gradually with increasing Tb^{3+} content, reaching its maximum when the Tb_4O_7 doping concentration attains 5 mol%.

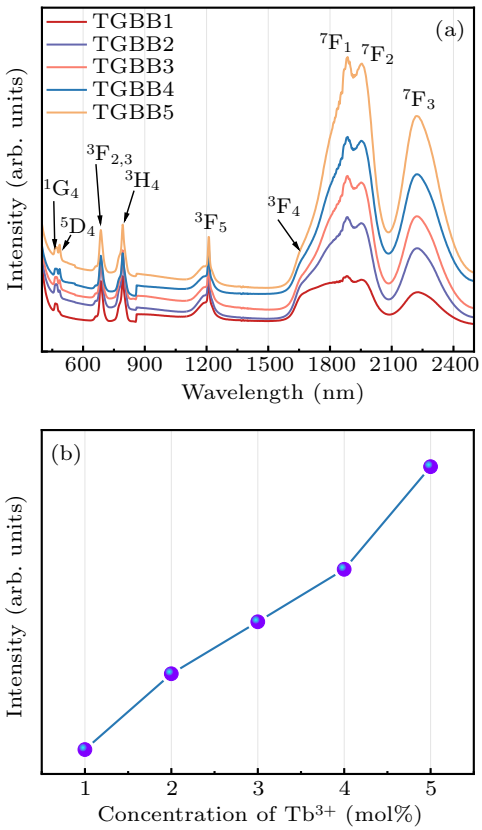


Fig. 4. Absorption spectra of the TGBB1–TGBB5 glass samples: (a) absorption spectra, (b) intensity of the $^7F_6 \rightarrow {}^7F_1$ transition peak as a function of Tb^{3+} doping concentration.

The Judd–Ofelt (JO) theory is widely utilized to characterize the spectral properties of crystalline materials and rare-earth (RE)-doped glasses.[49,50] Using the density and refractive index of the TGBB2 glass sample, the experimental oscillator strengths (f_{exp}) and theoretical oscillator strengths (f_{cal}) were computed from the integral values of the absorption peaks in the aforementioned absorption spectra and the reduced matrix elements of Tm^{3+} and Tb^{3+}. Further, the JO intensity parameters Ω_t ($t = 2, 4, 6$) for Tb^{3+} and Tm^{3+} in TGBB2 were determined by the least-squares method, with calculation results listed in Table 4.

Table 4. Judd–Ofelt intensity parameters of the TGBB2 glass and other glass systems (10^{-20} cm^2).

Matrix glass	Doped ions	Ω_2	Ω_4	Ω_6	χ	Ref.
TGBB2	Tm^{3+}	7.08	2.79	1.06	2.63	this work
	Tb^{3+}	0.98	9.89	5.84	1.69	this work
ZBLAN	Tm^{3+}	2.31	1.28	1.17	1.09	[28]
Bismuth	Tm^{3+}	5.00	1.13	1.17	0.97	[54]
Tellurite	Tm^{3+}	1.96	1.99	1.72	1.16	[55]

The root-mean-square (RMS) errors of the JO intensities for Tm^{3+}/Tb^{3+}-co-doped systems derived in this study are 3.13×10^{-7} and 1.42×10^{-7}, respectively. These minimal errors validate the reliability of the derived results. The Ω_2 parameter corresponds to the network configuration and ligand field symmetry of the glass matrix,[51] whereas Ω_4 correlates with the viscosity of the host glass matrix embedding rare-earth ions.[52] The larger Ω_4 intensity parameter of Tb^{3+} in

the TGBB2 sample suggests that the glass exhibits significant viscosity. Ω_6 is considered to be related to the medium rigidity: an increase in Ω_6 decreases medium rigidity, weakens the average force between Tm–O and Tb–O bonds, reduces Stark splitting of energy levels, and thus enhances the fluorescence emission spectra.[53] Furthermore, a spectral quality factor χ is proposed to evaluate the excitation–emission characteristics of activator ions in laser matrix materials, with its definition given by $\chi = \Omega_4/\Omega_6$. This parameter serves to characterize the application potential of rare-earth-doped glass materials within laser system configurations.[16] A higher χ value indicates more intense laser emission. Calculations reveal that the spectral quality factors χ for Tm^{3+} and Tb^{3+} in the TGBB2 glass sample are 2.63 and 1.69, respectively, which exceed the value of 1.09 in fluoride glass.[28] Meanwhile, the values of Ω_2, Ω_4, and Ω_6 in TGBB2 glass are all higher than those in fluoride matrix glass,[28] bismuthate glass,[54] and tellurite glass[55] with varying compositions.

Various radiative parameters of Tm^{3+} and Tb^{3+} in TGBB2 glass, including the spontaneous emission transition probability (A_{rad}), fluorescence branching ratio (β), and radiative lifetime (τ_{rad}), were computed using the JO theory. The results are tabulated in Table 5 and Table 6. The detailed calculation process is provided in our research group's previous study.[27] In general, a higher spontaneous emission transition probability (A_{rad}) implies stronger luminescent performance of the glass.[56] Furthermore, the high refractive index of tellurite glass contributes to the enhancement of its spontaneous emission transition probability. Thus, TGBB glass shows greater promise for achieving more efficient laser output. Meanwhile, the radiative lifetimes of the Tb^{3+}:$^5D_3$ and $^5D_4$ energy levels in the TGBB2 glass sample are 0.89 ms and 1.89 ms, respectively, while those of the Tm^{3+}:$^1G_4$ and $^1D_2$ energy levels are 0.23 ms and 0.02 ms, respectively, indicating a relatively strong energy storage capability. The calculation results indicate that TGBB2 glass is a viable gain material for blue–green fiber lasers.

Table 5. Relevant radiative parameters of Tm^{3+} in the TGBB2 glass sample.

Up transition	Down transition	Wavelength (nm)	A_{rad} (s^{-1})	ΣA (s^{-1})	β (%)	τ_{rad} (ms)
$^1G_4$	$^3F_2$	1488.0	21.95	3847.78	0.51	0.23
	$^3F_3$	1404.0	113.35		2.62	
	$^3F_4$	624.0	326.47		7.53	
	$^3H_4$	1106.0	592.03		13.66	
	$^3H_5$	750.0	1165.76		38.11	
	$^3H_6$	474.74	1628.22		37.57	
$^1D_2$	$^3F_2$	779.0	1018.57	41546.16	2.54	0.02
	$^3F_3$	747.0	2273.37		5.47	
	$^3F_4$	454.0	34048.98		81.95	
	$^3H_4$	651.0	3980.04		9.58	
	$^3H_5$	506.0	225.20		0.54	

Table 6. Relevant radiative parameters of Tb^{3+} in the TGBB2 glass sample.

Up transition	Down transition	Wavelength (nm)	A_{rad} (s^{-1})	ΣA (s^{-1})	β (%)	τ_{rad} (ms)
$^5D_3$	$^7F_5$	410	328.97	1121.26	29.34	0.89
	$^7F_4$	433	107.22		9.56	
	$^7F_3$	452	359.34		32.05	
	$^7F_2$	466	165.73		14.78	
	$^7F_1$	472	160.00		14.27	
$^5D_4$	$^7F_6$	486	112.93	528.68	21.36	1.89
	$^7F_5$	545	223.57		42.29	
	$^7F_4$	584	75.61		14.30	
	$^7F_3$	621	54.78		10.36	
	$^7F_2$	647	23.18		4.38	
	$^7F_1$	659	38.61		7.30	

3.3. Fluorescence spectra and lifetime analysis

Upon excitation by a 358-nm laser diode (LD), the fluorescence spectra of TGBB1–TGBB4 glass specimens within the wavelength interval of 400 nm–650 nm were documented, as shown in Fig. 5. The figure clearly displays two distinct sets of fluorescence emission peaks. The fluorescence emission peak at 452 nm corresponds to the energy-level transition of Tm^{3+}:$^1G_4 \rightarrow {}^3H_6$. The other group of four fluorescence emission peaks at 489 nm, 544 nm, 582 nm, and 620 nm corresponds to the energy-level transitions of Tb^{3+}:$^5D_4 \rightarrow {}^7F_6$, $^5D_4 \rightarrow {}^7F_5$, $^5D_4 \rightarrow {}^7F_4$, and $^5D_4 \rightarrow {}^7F_3$, respectively. As shown in Fig. 5(b), the intensity of the blue fluorescence emission peak of Tm^{3+} at 452 nm (Tm^{3+}:$^1G_4 \rightarrow {}^3H_6$) gradually decreases with the increase of Tb^{3+} concentration. However,

the intensity of the green fluorescence emission peak of Tb^{3+} at 544 nm (Tb^{3+}:$^5D_4 \rightarrow {}^7F_5$) gradually increases with the increase of Tb^{3+} concentration. When the Tb_4O_7 doping concentration is 2 mol%, the blue–green emission achieves equilibrium. This demonstrates that Tm^{3+} continuously sensitizes Tb^{3+} luminescence, with effective energy transfer occurring between the two ions (to be further investigated in the subsequent section). This finding suggests that TGBB2 glass represents a promising candidate for blue–green laser applications.

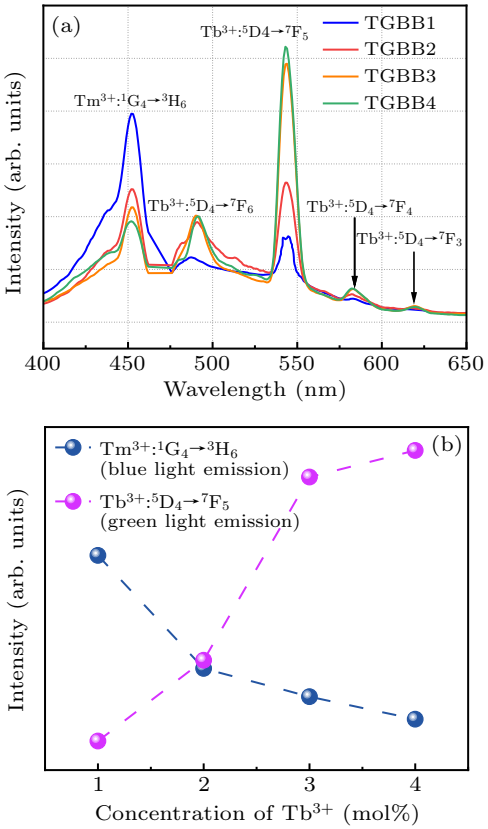


Fig. 5. Fluorescence emission spectra of the TGBB1–TGBB4 glass samples. (a) Fluorescence spectra, (b) variation of blue and green fluorescence emission peak intensities with Tb^{3+} doping concentration.

Additionally, the effective fluorescence bandwidth of the fluorescence spectrum (inhomogeneous broadening of rare-earth ions in aperiodic glass matrices) can qualitatively reflect the tunability of laser output. This parameter evaluates the bandwidth for rare-earth ion signal transmission and serves as a fundamental parameter for characterizing the amplification properties of rare-earth-doped glass samples. The calculation formula is as follows:[57]

$$\Delta\lambda_{\text{eff}} = \frac{\int I(\lambda)\,\mathrm{d}\lambda}{I_{\max}}. \tag{6}$$

In the equation, $\int I(\lambda)\,\mathrm{d}\lambda$ represents the integrated intensity of the fluorescence emission peak, and $I_{\max}$ denotes the peak maximum intensity. The calculated effective fluorescence bandwidths for TGBB2 glass at 452 nm and 544 nm are 7.46 nm and 6.69 nm, respectively.

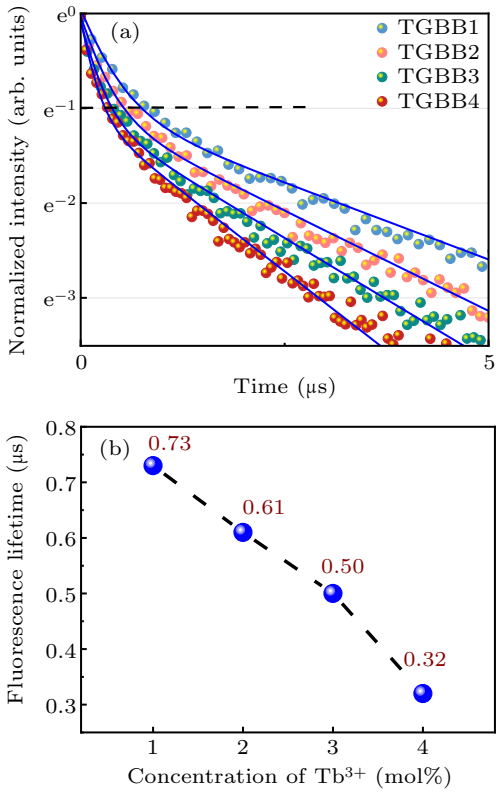


Fig. 6. Fluorescence decay curves of the TGBB1–TGBB4 glass samples: (a) Fluorescence lifetime decay profiles, (b) variation of sample lifetimes with Tb^{3+} concentration.

Figure 6 shows the measured decay curves of the Tm^{3+}:$^1G_4 \rightarrow {}^3H_6$ energy level transitions for the TGBB1–TGBB4 glass samples under 358-nm excitation. The decay curves of fluorescence lifetimes for rare-earth ions at specific energy levels in the glass specimens can be modeled using a double-exponential function[27]

$$I(t) = I_0 + A_1 \exp\left(-\frac{t}{\tau_1}\right) + A_2 \exp\left(-\frac{t}{\tau_2}\right). \tag{7}$$

In the formula, A_1 and A_2 are the fitting coefficients, τ_1 and τ_2 are the fluorescence lifetime values, $I(t)$ and I_0 represent the emission intensities at time t and the initial moment, respectively. In addition, the fluorescence lifetime can be calculated using the following equation[46]

$$\tau_{\text{mea}} = \frac{A_1\tau_1^2 + A_2\tau_2^2}{A_1\tau_1 + A_2\tau_2}. \tag{8}$$

The radiative lifetime (τ_{rad}) derived from JO theory and the experimentally measured fluorescence lifetime (τ_{mea}) enable the calculation of the glass sample's quantum efficiency (η) using the following equation[58]

$$\eta = \frac{\tau_{\text{mea}}}{\tau_{\text{rad}}} \times 100\%. \tag{9}$$

Following exponential fitting of the decay curves, the fluorescence lifetimes of the glass samples are 0.73 μs, 0.61 μs, 0.50 μs, and 0.32 μs, respectively. The calculated quantum efficiency for the Tm^{3+}:$^1G_4 \rightarrow {}^3H_6$ transition is 0.217%, which is low due to the sensitization of Tm^{3+}:$^1G_4$ to the Tb^{3+}:$^5D_4$

energy level. Additionally, the calculated energy transfer efficiency reaches 95.5%, indicating efficient energy transfer between the two ions.

Using the fluorescence emission spectral data under 358 nm excitation, figure 7 presents the CIE 1931 chromaticity diagram of the TGBB1–TGBB4 glass samples. By applying the color matching functions $X(\lambda)$, $Y(\lambda)$, and $Z(\lambda)$ at the excitation wavelength of 377 nm, the CIE chromaticity coordinates of the TGBB1–TGBB4 glass samples were calculated as (0.2031, 0.2143), (0.2145, 0.3032), (0.2237, 0.3560), and (0.2256, 0.3553), respectively. As clearly observed from the CIE 1931 chromaticity diagram, the emission color gradually shifts from blue to green with the increase in Tb^{3+} concentration, making it suitable as a gain medium for blue–green laser bands.

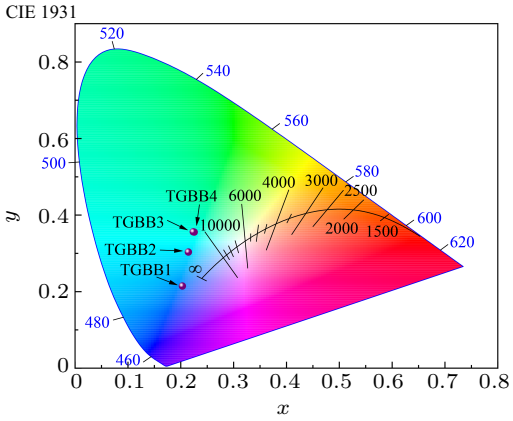


Fig. 7. CIE 1931 chromaticity diagram of the TGBB1–TGBB4 series glass samples.

Additionally, the color purity (CP) of the glass sample[59] serves as a crucial indicator for evaluating the optical properties of the glass, which is predominantly utilized to characterize the glass's selective transmission or reflection ability for specific light wavelengths. The calculation formula is expressed as follows:

$$CP = \sqrt{\frac{(x-x_{\mathrm{i}})^2+(y-y_{\mathrm{i}})^2}{(x_{\mathrm{d}}-x_{\mathrm{i}})^2+(y_{\mathrm{d}}-y_{\mathrm{i}})^2}} \times 100\%. \tag{10}$$

In this equation, (x, y) denote the chromaticity coordinates of the glass sample, $(x_{\mathrm{i}}, y_{\mathrm{i}})$ represent the chromaticity coordinates of standard white light (0.3333, 0.3333), and $(x_{\mathrm{d}}, y_{\mathrm{d}})$ signify the chromaticity coordinates of the dominant wavelength. For the dominant wavelength of 544-nm green light, the corresponding chromaticity coordinates are (0.3453, 0.5565). The calculated color purity (CP) values are presented in Table 7.

Table 7. CIE chromaticity coordinates and color purity of the TGBB1–TGBB4 series glass samples.

Glass	CIE_x	CIE_y	CP (%)
TGBB1	0.2031	0.2143	78.94
TGBB2	0.2145	0.3032	54.85
TGBB3	0.2237	0.3560	50.01
TGBB4	0.2256	0.3553	49.20

3.4. Analysis of absorption and emission cross-sections and gain performance

To explore the laser performance of TGBB2 glass, the absorption and emission cross-sections were calculated using the Beer–Lambert and Füchtbauer–Ladenburg (FL) formulas based on the absorption spectra, fluorescence spectra, and spontaneous emission transition probability (A_{rad})[60]

$$\sigma_{\mathrm{abs}} = \frac{2.303\mathrm{OD}(\lambda)}{N_0 l}, \tag{11}$$

$$\sigma_{\mathrm{emi}} = \frac{\lambda^5 A_{\mathrm{rad}} I(\lambda)}{8\pi c n^2 \int \lambda I(\lambda)\mathrm{d}\lambda}. \tag{12}$$

Furthermore, the stimulated emission cross-section can also be expressed using the McCumber theory equation and the calculated absorption cross-section[61]

$$\sigma_{\mathrm{emi}} = \sigma_{\mathrm{abs}} \frac{Z_{\mathrm{L}}}{Z_{\mathrm{U}}} \exp\left[\frac{hc}{kT}\left(\frac{1}{\lambda_{\mathrm{ZL}}}-\frac{1}{\lambda}\right)\right]. \tag{13}$$

In the formula above, $\mathrm{OD}(\lambda)$ denotes the optical density of the absorption band, N_0 represents the doping concentration of rare-earth ions, l is the sample thickness, $I(\lambda)$ is the fluorescence emission intensity at wavelength λ, A_{rad} is the spontaneous emission transition probability, c is the speed of light in vacuum, n is the refractive index of the glass, Z_{L} and Z_{U} are the partition functions of the lower and upper energy levels in the radiation process, respectively, k is the Boltzmann constant, T is the temperature in Kelvin, and λ_{ZL} is the energy difference between the upper and lower energy levels. Based on the above formulas, the absorption and emission cross-sections of the TGBB2 glass sample were calculated, as shown in Fig. 8.

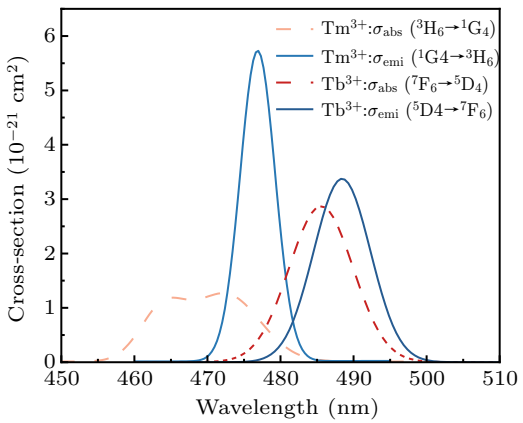


Fig. 8. Absorption and emission cross-sections of Tm^{3+}:$^1G_4 \rightarrow {}^3H_6$ and Tb^{3+}:$^5D_4 \rightarrow {}^7F_6$ transitions in TGBB2 glass sample.

The emission cross-section of a glass sample characterizes its laser emission capability and serves as a critical parameter for evaluating laser performance. The emission cross-section of Tm^{3+} exhibits a peak at 476 nm with a maximum value of 5.87×10^{-21} cm^2, indicating the substantial potential of TGBB2 glass for blue-light laser emission. The calculated maximum absorption cross-section of Tm^{3+} is 1.47 ×

10^{-21} cm^2. For Tb^{3+}, the absorption cross-section is centered at ~ 486 nm with a value of 2.97×10^{-21} cm^2, while the maximum emission cross-section attains 3.37×10^{-21} cm^2, validating the robust green-light laser emission performance of TGBB2 glass. Notably, the emission cross-section of Tm^{3+} overlaps with the absorption cross-section of Tb^{3+}, confirming the energy transfer process between Tm^{3+} and Tb^{3+}. The integration of the overlapping area facilitates an in-depth investigation of the microscopic energy transfer mechanism. Furthermore, the figure of merit (FOM) of glass samples serves as a key parameter for assessing the laser performance of rare-earth-doped glass, which is employed to quantify the comprehensive efficiency and application potential of materials in laser systems. It is calculated using the following formula:[62]

$$\mathrm{FOM} = \sigma_{\mathrm{emi}} \times \tau_{\mathrm{mea}}. \tag{14}$$

In the aforementioned formula, τ_{mea} represents the measured fluorescence lifetime of the glass sample (0.61 μs), and σ_{emi} denotes the calculated emission cross-section (5.87×10^{-21} cm^2). The calculated figure of merit (FOM) for the TGBB2 glass sample is 8.97×10^{-27} cm^2·s, suggesting that TGBB2 glass enables a broader gain frequency bandwidth. When utilized in blue–green laser systems, this glass is anticipated to facilitate higher transmission rates.

Based on the calculated values of the rare-earth ion absorption cross-section (σ_{abs}) and emission cross-section (σ_{emi}), the gain coefficient of the TGBB2 glass sample can be calculated using the following formula[63]

$$G(\lambda) = N[P\sigma_{\mathrm{emi}}(\lambda) - (1-P)\sigma_{\mathrm{abs}}(\lambda)]. \tag{15}$$

Here, P denotes the proportion of the population in the upper laser level to the total population. The calculated gain coefficients of the TGBB2 glass sample are presented in Fig. 9.

As illustrated in the figure, the gain peaks of both ions display blue shifts of varying degrees, which is typical of a three-level emission system. The gain wavelength of Tm^{3+} is centered at ~ 476 nm with a maximum gain coefficient of 2.98 cm^{-1}, whereas that of Tb^{3+} is at ~ 487 nm with a maximum gain coefficient of 0.46 cm^{-1}. Notably, Tm^{3+} first achieves positive gain at a gain coefficient of 0.4. The capability to generate positive gain at such a low P value suggests that Tm^{3+} in the TGBB2 glass sample exhibits a low laser threshold, thereby facilitating laser emission as a blue–green laser material.

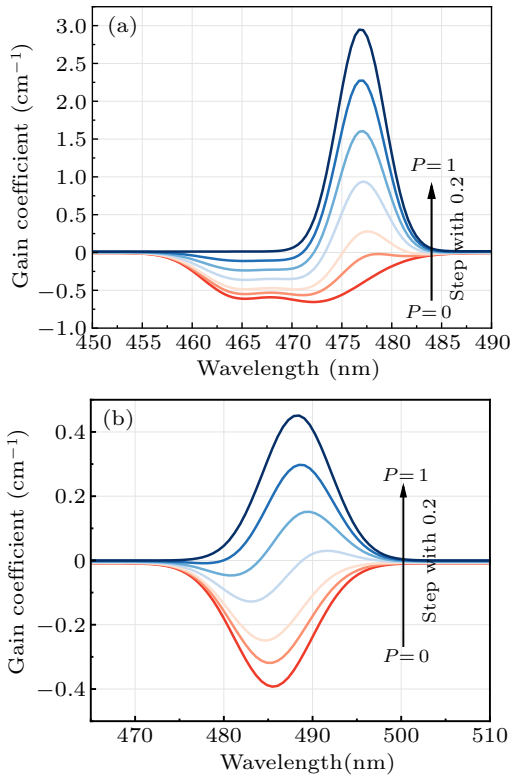


Fig. 9. Gain coefficient curves of the TGBB2 glass sample: (a) gain coefficient curve for the Tm^{3+}:$^1G_4 \rightarrow {}^3H_6$ transition, (b) gain coefficient curve for the Tb^{3+}:$^5D_4 \rightarrow {}^7F_6$ transition.

Table 8 presents a comparison of key laser parameters (emission cross-section, gain coefficient, figure of merit, thermal stability, *etc.*) between Tm^{3+}/Tb^{3+} co-doped TeO_2–GeO_2–Bi_2O_3–BaF_2 glass and other conventional host glasses.

Table 8. Comparisons of key laser parameters for host glasses.

Parameter	σ_{emi} (10^{-21} cm^2)	FOM (cm^2·s)	$G(\lambda)$ (cm^{-1})	ΔT (°C)	Ref.
TGBB2	Tm^{3+}:5.87 Tb^{3+}:3.37	8.97×10^{-27}	Tm^{3+}:2.98 Tb^{3+}:0.46	117	this work
ZBLAN	Tm^{3+}:2.35	2.36×10^{-27}	Tm^{3+}:0.71	76	[28]
Bismuthate	Tb^{3+}:2.01	3.59×10^{-27}	Tb^{3+}:2.92	102	[46]

3.5. Energy transfer mechanism and microparameter analysis

Figure 10 depicts the energy transfer mechanism in Tm^{3+}/Tb^{3+}-co-doped TGBB2 glass. Upon excitation by an 808-nm laser diode (LD), electrons in the Tm^{3+}:$^3H_6$ energy level are excited to the $^1D_2$ level. Subsequently, a portion of electrons at the $^1D_2$ level undergoes radiative relaxation to the $^3F_4$ level, emitting 486 nm fluorescence. The remaining electrons undergo non-radiative relaxation to the metastable $^1G_4$ level. At this stage, the Tm^{3+}:$^1G_4$ level transfers partial energy to the Tb^{3+}:$^5D_4$ level, followed by decay to the $^3H_6$ level, resulting in 452 nm fluorescence emission. The specific energy transfer process is described as: (ET: Tm^{3+}:$^1G_4$ + Tb^{3+}:$^7F_6 \rightarrow Tm^{3+}$:$^3H_6$ + Tb^{3+}:$^5D_4$). Elec-

trons at the Tb^{3+}:$^5D_4$ level undergo radiative relaxation to the ground-state $^7F_6$ level, yielding 544-nm green light emission. The energy transfer from Tm^{3+} to Tb^{3+} follows Dexter's electron exchange mechanism:[64] the minor energy mismatch between Tm^{3+}: $^1G_4$ and Tb^{3+}:$^5D_4$ can be compensated by the phonon energy of the matrix (763 cm^{-1}), thereby enabling resonant transfer. Microscopically, this transfer occurs between Tm^{3+} and Tb^{3+} ions within a small critical distance (R_C): electrons in the 4f orbitals of Tm^{3+} exchange with those in the 4f orbitals of Tb^{3+}, completing energy transfer without photon emission. The low multi-phonon contribution (4.7% for one-phonon assistance, Table 9) confirms that this process is dominated by zero-phonon resonant transfer. When Tb^{3+} concentration exceeds 2 mol%, the average Tm^{3+}–Tb^{3+} distance decreases below the critical distance (R_C), triggering Tb^{3+}–Tb^{3+} cross-relaxation ($^5D_4$+$^7F_6$ →$^7F_6$+ ^5D_J) and resulting in slight quenching of emission intensity.

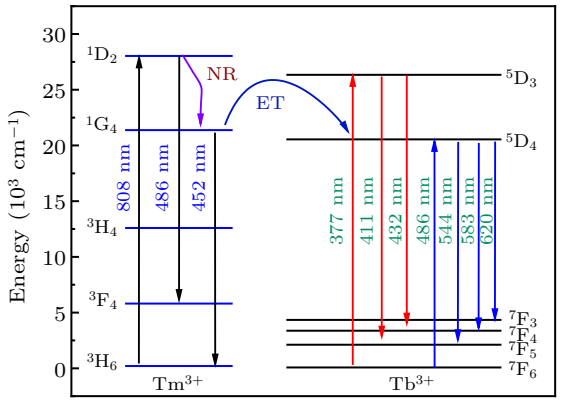


Fig. 10. Schematic diagram of Tm^{3+}/Tb^{3+} energy transfer under 808-nm excitation.

Microscopic parameters of energy transfer were estimated based on the Forster and Dexter theories.[64] The energy transfer rate from the donor (D) Tm^{3+} to the acceptor (A) Tb^{3+} can be expressed as

$$W_{\mathrm{D-A}} = \left(\frac{2\pi}{h}\right)|H_{\mathrm{DA}}|^2 S_{\mathrm{DA}}^N. \tag{16}$$

In the formula, $|H_{\mathrm{DA}}|$ is the Hamiltonian matrix element between the upper and lower energy levels during energy transfer; S_{DA}^N is the overlap integral between the m-phonon emission sideband of Tm^{3+} and the k-phonon absorption sideband of Tb^{3+}; N is the total number of phonons involved in energy transfer. Based on the Dexter theory, the phonon-assisted energy transfer rate between rare-earth ions can be further expressed as

$$W_{\mathrm{D-A}} = \frac{C_{\mathrm{D-A}}}{R^6} = \frac{R_{\mathrm{C}}^6}{R_{\tau_{\mathrm{D}}}^6}, \tag{17}$$

where $C_{\mathrm{D-A}}$ is the energy transfer coefficient, τ_{D} is the excited state lifetime of Tm^{3+}, R is the distance between Tm^{3+} and Tb^{3+}, and R_{C} represents the critical distance for interaction between Tm^{3+} and Tb^{3+}, with the calculation formula as follows:

$$R_{\mathrm{C}}^6 = \frac{6c\tau_{\mathrm{D}} g_{\mathrm{low}}^{\mathrm{D}}}{(2\pi)^4 n^2 g_{\mathrm{up}}^{\mathrm{D}}} \sum_{N=0}^{\infty}\sum_{m=0}^{N}\int \sigma_{\mathrm{emi}(k-\mathrm{phonon})}^{\mathrm{D}}(\lambda) \times \sigma_{\mathrm{abs}(k-\mathrm{phonon})}^{\mathrm{A}}(\lambda)\,\mathrm{d}\lambda. \tag{18}$$

In the above formula, c and n represent the speed of light and the refractive index of the glass sample, respectively; $g_{\mathrm{up}}^{\mathrm{D}}$ and $g_{\mathrm{low}}^{\mathrm{D}}$ denote the degeneracies of the upper and lower energy levels of Tm^{3+} ions, respectively; $\sigma_{\mathrm{emi}(m\text{-phonon})}^{\mathrm{D}}$ and $\sigma_{\mathrm{abs}(k\text{-phonon})}^{\mathrm{A}}$ represent the m-phonon emission sideband of Tm^{3+} and the k-phonon absorption sideband of Tb^{3+}, which are calculated by the following formulas:[65]

$$\sigma_{\mathrm{emi}(m\text{-phonon})}^{\mathrm{D}} = \sigma_{\mathrm{emi}}^{\mathrm{D}}(\lambda_m^+) \approx \frac{s_0^m e - s_0}{m!}(\bar{n}+1)^m \times \sigma_{\mathrm{emi}(\mathrm{exp}t)}^{\mathrm{D}}(E - mh\omega_0), \tag{19}$$

$$\sigma_{\mathrm{abs}(k-\mathrm{phonon})}^{\mathrm{A}} = \sigma_{\mathrm{abs}}^{\mathrm{A}}(\lambda_k^-) \approx \frac{s_0^k e - s_0}{k!}(\bar{n})^k \times \sigma_{\mathrm{abs}(\mathrm{exp}t)}^{\mathrm{A}}(E + kh\omega_0). \tag{20}$$

In the above formula, $\lambda_m^+ = \frac{1}{1/\lambda - mh\omega_0}$ and $\lambda_k^- = \frac{1}{1/\lambda + kh\omega_0}$ represent the wavelengths corresponding to the m-phonon emission of Tm^{3+}, and the k-phonon absorption of Tb^{3+}, respectively; $\bar{n} = \frac{1}{\exp(h\omega_0/KT)-1}$ denotes the average occupancy of phonon modes at temperature T, S_0 is the Huang–Rhys factor, and $h\omega_0$ is the maximum phonon energy of the glass. When only considering the m-phonon emission of Tm^{3+} (*i.e.*, $N = m$), the energy transfer probability between Tm^{3+} and Tb^{3+} is

$$W_{\mathrm{D-A}}(R) = \frac{6cg_{\mathrm{low}}^{\mathrm{D}}}{(2\pi)^4 n^2 R^6 g_{\mathrm{up}}^{\mathrm{D}}} \sum_{N=0}^{\infty}\sum_{k=0}^{N} P_{(N-k)}^{+} P_k^{-} P_k^{+} \times \int \sigma_{\mathrm{emi}}^{\mathrm{D}}(\lambda_N^+)\,\sigma_{\mathrm{abs}}^{\mathrm{A}}(\lambda)\,\mathrm{d}\lambda. \tag{21}$$

In the formula, $\sigma_{\mathrm{emi}}^{\mathrm{D}}(\lambda_N^+)$ and $\sigma_{\mathrm{abs}}^{\mathrm{A}}(\lambda)$ denote the emission sideband of Tm^{3+} after emitting N phonons and the absorption cross-section of Tb^{3+}, respectively; $P_{(N-k)}^{+}$ and P_k^{-} represent the probabilities of Tm^{3+} emitting N–k phonons and Tb^{3+} absorbing k phonons, respectively, which can be calculated by the following formulas:

$$P_{(N-k)}^{+} \cong \exp\left[-(2\bar{n}+1)S_0\right]\frac{S_0^{(N-k)}}{(N-k)!}(\bar{n}+1)^{N-k}, \tag{22}$$

$$P_k^{-} \cong \exp\left[-2\bar{n}S_0\right]\frac{S_0^k}{k!}(\bar{n})^k. \tag{23}$$

Thus, the forward and backward energy transfer coefficients $C_{\mathrm{D-A}}$ and $C_{\mathrm{A-D}}$ between Tm^{3+} and Tb^{3+}, as well as the proportion of phonon-assisted contributions, can be obtained using the following formulas:[66]

$$C_{\mathrm{D-A}} = \frac{6cg_{\mathrm{low}}^{\mathrm{D}}}{(2\pi)^4 n^2 g_{\mathrm{up}}^{\mathrm{D}}} \sum_{N=0}^{\infty}\sum_{k=0}^{N} P_{(N-k)}^{+} P_k^{-} P_k^{+}$$

$$\times \int \sigma_{\mathrm{emi}}^{\mathrm{D}}\left(\lambda_N^{+}\right)\sigma_{\mathrm{abs}}^{\mathrm{A}}\left(\lambda\right)\mathrm{d}\lambda, \tag{24}$$

$$C_{\mathrm{A-D}} = \frac{6cg_{\mathrm{low}}^{\mathrm{A(D)}}}{(2\pi)^4 n^2 g_{\mathrm{up}}^{\mathrm{A(D)}}} \sum_{N=0}^{\infty}\sum_{k=0}^{N} P_{(N-k)}^{+} P_k^{-} P_k^{+} \times \int \sigma_{\mathrm{emi}}^{\mathrm{A}}\left(\lambda_N^{-}\right)\sigma_{\mathrm{abs}}^{\mathrm{D}}\left(\lambda\right)\mathrm{d}\lambda, \tag{25}$$

$$R_1 = \frac{S_{\mathrm{DA}}^{N} P_{(N-k)}^{+} P_k^{-} P_k^{+}}{\sum_{N=0}^{\infty}\sum_{k=0}^{N} S_{\mathrm{DA}}^{N} P_{(N-k)}^{+} P_k^{-} P_k^{+}}, \tag{26}$$

$$R_2 = \frac{S_{\mathrm{AD}}^{N} P_{(N-k)}^{-} P_k^{+} P_k^{-}}{\sum_{N=0}^{\infty}\sum_{k=0}^{N} S_{\mathrm{AD}}^{N} P_{(N-k)}^{-} P_k^{+} P_k^{-}}. \tag{27}$$

In the formula, R_1 and R_2 represent the proportions of different phonon numbers in the forward and backward energy transfer processes, respectively. Figure 11 shows the phonon emission sideband diagram calculated in this work, where panel (a) represents the forward energy transfer (*i.e.*, Tm^{3+}:$^1G_4$ →Tb^{3+}:$^5D_4$), and panel (b) illustrates the backward energy transfer process (*i.e.*, Tb^{3+}:$^5D_4$ →Tm^{3+}:$^1G_4$).

Based on the absorption and emission cross-sections of Tm^{3+} and Tb^{3+} in the TGBB2 glass sample together with the phonon emission sidebands, Table 9 lists the microscopic energy transfer parameters between Tm^{3+} and Tb^{3+} derived from the phonon emission sideband theory. The results indicate that in the forward energy transfer process, zero-phonon energy constitutes the vast majority (95.3%) of energy transfer, whereas one-phonon energy accounts for only 4.7%, confirming that forward energy transfer primarily occurs without phonon energy assistance. In the backward energy transfer process, zero-phonon energy transfer reaches 99.99%, virtually dominating the entire process, whereas one-phonon energy transfer is nearly undetectable, validating that backward energy transfer scarcely relies on phonons. Furthermore, the calculated $C_{\mathrm{D-A}}$ value is 571.83×10^{-40} cm^6/s, and $C_{\mathrm{A-D}}$ is 63.12×10^{-40} cm^6/s. The significantly larger $C_{\mathrm{D-A}}$ compared to $C_{\mathrm{A-D}}$ confirms that Tm^{3+} sensitizes Tb^{3+} luminescence, with an energy transfer rate of 442.90×10^{-20} cm^3/s. Moreover, the calculated $C_{\mathrm{D-D}}$ is 7.64×10^{-40} cm^6/s, which is negligible in comparison to $C_{\mathrm{D-A}}$ and $C_{\mathrm{A-D}}$, indicating that energy transfer between Tm^{3+} ions is minimal, thereby preventing energy loss. Notably, while zero-phonon energy transfer dominates (82.18%) in Tm^{3+}–Tm^{3+} energy transfer, one-phonon energy transfer accounts for 17.82%, which is non-negligible, indicating partial involvement of phonon-assisted energy transfer in Tm^{3+}–Tm^{3+} interactions.

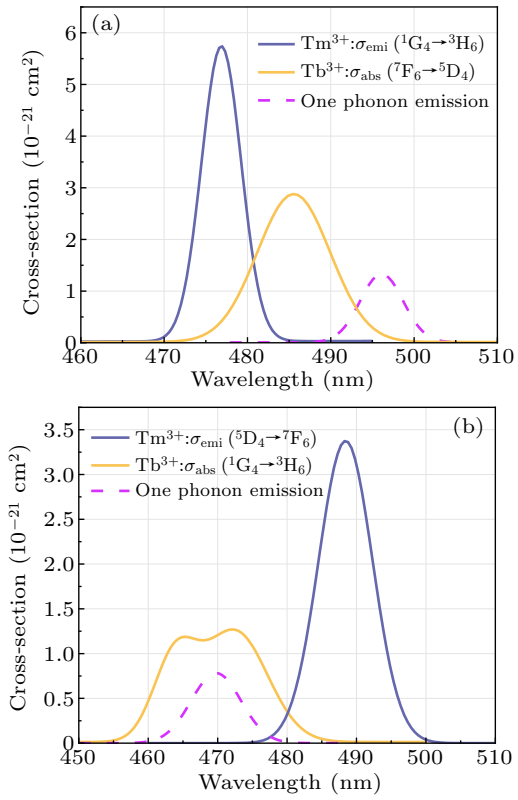


Fig. 11. Absorption and emission cross-sections of Tm^{3+} and Tb^{3+} with corresponding phonon emission sidebands in the TGBB2 glass sample: (a) forward energy transfer: Tm^{3+}:$^1G_4$ →Tb^{3+}:$^5D_4$, (b) backward energy transfer: Tb^{3+}:$^5D_4$ →Tm^{3+}:$^1G_4$.

Table 9. Microscopic energy transfer parameters between Tm^{3+} and Tb^{3+} in the TGBB2 glass sample.

Glass	ET	Phonon number (N) and phonon assisted contribution (%)		Transfer constant (10^{-40} cm^6/s)
TGBB2	Tm^{3+}:$^1G_4$ →Tm^{3+}:$^1G_4$	0 82.18	1 17.82	$C_{\mathrm{D-D}} = 7.64$
	Tm^{3+}:$^1G_4$ →Tb^{3+}:$^5D_4$	0 95.30	1 4.70	$C_{\mathrm{D-A}} = 571.83$
	Tb^{3+}:$^5D_4$ →Tm^{3+}:$^1G_4$	0 99.99	1 0.01	$C_{\mathrm{A-D}} = 63.12$

Furthermore, the energy transfer rate (W_{ET}) is calculated using the following formula:[67]

$$W_{\mathrm{ET}} = 13\left(C_{\mathrm{D-A}}\right)^{1/2}\left(C_{\mathrm{D-D}}\right)^{1/2} N_{\mathrm{D}}. \tag{28}$$

In the equation, N_{D} denotes the Tm^{3+} ion concentration. The calculated W_{ET} for Tm^{3+} → Tb^{3+} energy transfer in TGBB2 glass is 442.90×10^{-20} cm^3/s.

4. Conclusion

In this study, a matrix glass with the composition $70TeO_2$–$5GeO_2$–$5Bi_2O_3$–$20BaF_2$ and Tm^{3+}/Tb^{3+}-co-doped $70TeO_2$–$5GeO_2$–$5Bi_2O_3$–$20BaF_2$–$0.75Tm_2O_3$–xTb_4O_7 (x =

1, 2, 3, 4, 5 mol%) glass samples were synthesized via high-temperature melt-quenching. The structure and physical properties of the matrix glass were tested and analyzed. The test results show that the density and refractive index of the matrix glass TGBB are 4.9702 g/cm^3 and 1.8341, respectively. Raman spectroscopy analysis indicates that the glass has a low phonon energy (763 cm^{-1}). DSC curve analysis gives the glass transition temperature $T_g = 396$ °C and crystallization temperature $T_x = 513$ °C, with a thermal stability interval $\Delta T = 117$ °C, demonstrating excellent thermal stability of the matrix glass TGBB. Subsequently, the fluorescence emission characteristics in the blue–green wavelength range were investigated. When the doping ratio of Tm_2O_3:Tb_4O_7 is 3:8, the TGBB2 glass sample exhibits balanced blue fluorescence at 452 nm and green fluorescence at 544 nm. Based on the JO theory, the calculated spontaneous emission transition probability (A_{rad}) and radiative lifetime (τ_{rad}) for Tm^{3+}:$^1G_4 \rightarrow {}^3H_6$ are 1628.22 s^{-1} and 0.23 ms, respectively; those for Tb^{3+}:$^5D_4 \rightarrow {}^7F_5$ are 223.57 s^{-1} and 1.89 ms, respectively. Furthermore, the maximum absorption cross-sections of Tm^{3+} and Tb^{3+} in TGBB2 glass are 5.87×10^{-21} cm^2 (476 nm) and 2.97×10^{-21} cm^2 (486 nm), respectively; the maximum gain coefficients $G(\lambda)$ are 2.98 cm^{-1} and 0.46 cm^{-1}, respectively. Further studies show that the forward energy transfer coefficient (Tm^{3+}: $^1G_4 \rightarrow Tb^{3+}$:$^5D_4$) is 571.83×10^{-40} cm^6/s, which is significantly higher than the backward energy transfer coefficient (Tb^{3+}:$^5D_4 \rightarrow Tm^{3+}$:$^1G_4$, 63.12×10^{-40} cm^6/s). The energy transfer rate (W_{ET}) is 442.90×10^{-20} cm^3/s, and the energy transfer efficiency reaches 99.5%. These findings confirm that the glass with the composition $70TeO_2$–$5GeO_2$–$5Bi_2O_3$–$20BaF_2$–$0.75Tm_2O_3$–$2Tb_4O_7$ (TGBB2) is the optimal luminescent material for blue–green wavelength applications.

Acknowledgement

Project supported by the Natural Science Foundation of Jilin Province, China (Grant No. YDZJ202401333ZYTS).

References

[1] Schirripa S G, Cozzella L and Leccese F 2020 *Sensors* **20** 2261
[2] Zhu S J, Chen X W, Liu X Y, Zhang G Q and Tian P F 2020 *Progress in Quantum Electronics* **73** 100274
[3] Duntley S Q 1963 *J. Opt. Soc. Am.* **53** 214
[4] Tsai C W, Yu C C, Huai Y W, Cheng T T and Gong R L 2017 *Sci. Rep.* **7** 40480
[5] Tian R Y, Wang T, Shen X Y, Zhu R J, Jiang L D, Lu Y L, Lu H Y, Song Y R and Zhang P 2024 *Sensors* **24** 2609
[6] Oubei H M, Duran J R, Bilal J J, Wang H Y, Tsai C T, Chi Y C, Ng T K, Kuo H C, He J H, Alouini M S, Gong R L and Boon S O 2015 *Opt. Express* **23** 23302
[7] Bünzli J C G 2006 *Accounts of Chemical Research* **39** 53
[8] Lai F Q, Xu X N, Shen J W, Wang Y H, Yan Y N, Nie Y W, You W X, Wu D, Han L and Xiao Z L 2023 *Silicon* **15** 1913
[9] Biswas K, Balaji S, Ghosh D, Atul D, Sontakke A D and Annapurna K 2014 *J. Alloys Compd.* **608** 266
[10] Su Q, Pei Z W, Chi L S, Zhang H J, Zhang Z Y and Zou F 1993 *J. Alloys Compd.* **192** 25
[11] Hegde V, Vighnesh K R, Kamath S D, Viswanath C S D, Almuqrin A H, Sayyed M I, Gangareddy J, Rajaramakrishna R and Keshavamurthy K 2024 *Appl. Phys. A* **130** 411
[12] Kucuk N, Kaynar Ü H, Akca S, Alajlani Y, Yin L, Wang Y, Guinea J G, Bulcar K, Dogan T, Karabulut Y, Ayvacikli M, Canimoglu A, Topaksu M and Can N 2020 *J. Alloys Compd.* **838** 155587
[13] Kashif I and Ratep A 2025 *Journal of Fluorescence* **35** 343
[14] Shen T H, Guo J F, Liang H X, Li Y L, Li K W, Dai Y H and Ai Y 2023 *Photonics* **10** 1238
[15] Castiglia A, Malinverni M, Rossetti M, Duelk M and Velez C 2021 *IEEE Photonics Technology Lett.* **33** 1235
[16] Zhang C, Han K X, Wu T, Zhou D C, Wang S B and Liu M 2023 *Ceramics International* **49** 14497
[17] Qin F J, Cong Y X, Zhou D C, Han K X, Ban Y M, Leng Z and Shao Z H 2024 *J. Alloys Compd.* **1009** 177044
[18] Zhou D C, Bai X M and Zhou H 2017 *Sci. Rep.* **7** 44747
[19] Cao J L, Wu Y X, Cong Y X, Bai Y R, Zhou D C, Ban Y M and Liao Y 2024 *Infrared Physics & Technology* **141** 105507
[20] Wang C Z, Tian Y, Gao X Y, Liu Q H, Huang F F, Li B P, Zhang J J and Xu S Q 2018 *Journal of Luminescence* **194** 791
[21] Wei Y L, Zhao J B, Fuhrmann S, Sajzew R, Wondraczek L and Ebendorff-Heidepriem H 2023 *Light: Science & Application* **12** 293
[22] Wei T, Chen F Z, Jing X F, Wang F C, Tian Y and Xu S Q 2014 *Solid State Sciences* **31** 5
[23] Farahinia L, Rezvani M and Rezazadeh M 2021 *Materials Research Bulletin* **139** 111265
[24] Swapna K, Mahamuda S, Rao A S, Jayasimhadri M, Shakya S and Prakash G V 2014 *Journal of Luminescence* **156** 180
[25] Huang B, Xu C F, Zhang Z, Zang C Y and Sun L Z 2018 *Journal of Non-Crystalline Solids* **502** 97
[26] Poulain M 2024 *APL Photonics* **9** 91103
[27] Pang R Z, Wu T, Han K X, Zhou Z Y, Zheng W, Kang B, Guo L X, Xie W T, Zhou D C and Leng Z 2025 *Ceramics International* **51** 27012
[28] Doualan J L, Girard S, Haquin H, Adam J L and Montagne J 2003 *Opt. Mater.* **24** 563
[29] Lu Z P and Liu C T 2003 *Phys. Rev. Lett.* **91** 115505
[30] Saad M and Poulain M 1987 *Materials Science Forum. Trans Tech Publications Ltd.* **19** 11
[31] Hrubý y A 1972 *Czechoslovak Journal of Physics B* **22** 1187
[32] Tian Y, Xu R R, Hu L L and Zhang J J 2012 *Journal of Quantitative Spectroscopy and Radiative Transfer* **113** 87
[33] Han K X, Zhang P, Wang S B, Guo Y Y, Zhou D C and Yu F X 2016 *Sci. Rep.* **6** 1
[34] Lin H, Wang X Y, Li C M, Yang H X, Pun E Y B and Tanabe S 2008 *Journal of Luminescence* **128** 74
[35] Souri D 2015 *Physica B* **456** 185
[36] Baldi G, Fontana A, Rossi F and Monaco G 2011 *Philosophical Magazine* **91** 1801
[37] Knoblochova K, Ticha H, Schwarz J and Tichy L 2009 *Opt. Mater.* **31** 895
[38] Guery G, Fargues A, Cardinal T, Dussauze M, Adamietz F, Rodriguez V, Musgraves J D, Richardson K and Thomas P 2012 *Chem. Phys. Lett.* **554** 123
[39] Rachkovskaya G E and Zakharevich G B 2007 *Journal of Applied Spectroscopy* **74** 86
[40] Shaltout I, Tang Y I, Braunstein R and Abu-elazm A M 1995 *Journal of Physics and Chemistry of Solids* **56** 141
[41] Heo J, Lam D, Sigel Jr G H, Mendoza E A and Hensley D A 1992 *Journal of the American Ceramic Society* **75** 277
[42] Zhang C, Han K X, Zhou D C, Xu P F, Cao J L, Song C L, Huang C Q and Qiang S 2022 *Journal of Luminescence* **249** 119055
[43] Koepke C, Wisniewski K, Środa M and Zelechower M 2020 *J. Alloys Compd.* **825** 154091
[44] Liao M, Hu L, Duan Z, Zhang L and Wen L 2007 *Appl. Phys. B* **86** 83
[45] Zhang Z, Skripka A, Dahl J C, Dun C C, Urban J J, Jaque D, Schuck P J, Cohen B E and Chan E M 2023 *Angewandte Chemie International Edition* **135** 2549
[46] Wu T, Hu J J, Han K X, Zhang C, Li M L, Pang R Z, Hu Y and Zhou D C 2023 *Ceramics International* **49** 11718
[47] Klimesz B, Lisiecki R and Ryba-Romanowski W 2020 *J. Alloys Compd.* **823** 153753

[48] Chen R, Tian Y, Li B P, Wang F C, Jing X F, Zhang J J and Xu S Q 2015 *Opt. Mater.* **49** 116

[49] Judd B R 1962 *Phys. Rev.* **127** 750

[50] Ofelt G S 1962 *J. Chem. Phys.* **37** 511

[51] Ratnakaram Y C, Naidu D T, Vijayakumar A and Rao J L 2004 *Opt. Mater.* **27** 409

[52] Lalla E A, Konstantinidis M, De S I, Martin I R, Lavin V and Rodríguez-Mendoza U R 2020 *J. Alloys Compd.* **845** 156028

[53] Jørgensen C K and Reisfeld R 1983 *Journal of the Less Common Metals* **93** 107

[54] Song X Y, Han K X, Zhou D C, Xu P F and Zhang P 2021 *Journal of Non-crystalline Solids* **557** 120575

[55] Xu R, Tian Y, Hu L and Zhang J 2011 *Appl. Phys. B* **104** 839

[56] Mallawany R E, Yousef S A, Shaer A E, Marzouk S and Elabd H A 2024 *JOJ Material Science* **8** 555739

[57] Nandi P and Jose G 2006 *Physica B* **381** 66

[58] Zhou Z Y, Zhang C, Han K X, Wu T and Zhou D C 2024 *Ceramics International* **50** 35782

[59] Sasikala T, Moorthy L R and Babu A M 2013 *Spectrochimica Acta Part A: Molecular and Biomolecular Spectroscopy* **104** 445

[60] Zhang C, Han K X, Wu T, Qiang S, Wu Q R, Yu M H, Li Q D and Wang Y H 2022 *Ceramics International* **48** 30546

[61] Zhang C, Han K X, Wu T, Qiang S, Wu Q R, Yu M H, Li Q D and Wang Y H 2022 *Ceramics International* **48** 30546

[62] Sardar D K, Nash K L, Yow R M and Gruber J B 2006 *J. Appl. Phys.* **100** 3108

[63] Zhang C, Han K X, Zhou D C, Song C L, Xu P F, Wu T, Huang C Q, Qiang S and Wu Q R 2022 *J. Alloys Compd.* **901** 163592

[64] Murphy C B, Zhang Y, Troxler T, Ferry V, Martin J J and Jones W E 2004 *J. Phys. Chem. B* **108** 1537

[65] Tarelho L V G, Gomes L and Ranieri I M 1997 *Phys. Rev. B* **56** 14344

[66] Miyakawa T and Dexter D L 1970 *Phys. Rev. B* **1** 2961

[67] De Sousa D F and Nunes L A O 2002 *Phys. Rev. B* **66** 24207